Climate Dynamics (2022) 59:1953–1968
https://doi.org/10.1007/s00382-022-06190-8

Extreme Indian Ocean dipole events associated with El Niño and Madden–Julian oscillation

Zongci Huang[1] · Wenjun Zhang[1] · Chao Liu[1] · Malte F. Stuecker[2]

Received: 15 August 2021 / Accepted: 2 February 2022 / Published online: 25 February 2022
© The Author(s), under exclusive licence to Springer-Verlag GmbH Germany, part of Springer Nature 2022

Abstract
The three strongest positive Indian Ocean dipole (pIOD) events over the past four decades occurred in 1994, 1997, and 2019 and caused severe social-economic impacts in the Indian Ocean (IO) rim countries. These three strongest positive pIOD events exhibited similar oceanic and atmospheric anomaly patterns during their mature phase, though with different physical origins. The extreme amplitudes of these pIOD events were closely related to concurrent El Niño or Madden–Julian oscillation (MJO) activity. For the 1997 extreme pIOD case, the concurrent extreme El Niño in the Pacific triggered strong easterly wind anomalies over the equatorial IO and therefore favored the rapid growth of the pIOD via intense upwelling along the Sumatra-Java coast. In contrast, the long stalled MJO convective anomalies over the western IO exerted an important role in the 2019 extreme pIOD event especially during September–October by causing easterly anomalies over the equatorial IO. During that year, the Pacific moderate warming had likely a small impact since no strong associated convection was present over the western and central equatorial Pacific due to the small amplitude of the Pacific sea surface temperature anomalies. Different from the 1997 and 2019 cases, both El Niño conditions in the Pacific as well as MJO activity over the western IO contributed to the 1994 extreme pIOD event. Our results emphasize that MJO activity should be considered as one physical drivers for the extreme pIOD event in addition to the traditional El Niño-associated forcing.

Keywords Indian Ocean dipole · Extreme event · El Niño · Madden–Julian oscillation

1 Introduction

The Indian Ocean dipole (IOD), characterized by opposite sea surface temperature (SST) anomalies between the tropical western Indian Ocean (WIO) and the eastern Indian Ocean (EIO), is the prominent year-to-year climate variability in the tropical Indian Ocean (e.g., Saji et al. 1999; Webster et al. 1999). It usually develops in boreal summer, matures in autumn, and rapidly decays in winter (Saji et al. 1999; Li et al. 2003; Saji and Yamagata 2003b). The climate response to the IOD is the most evident in Indian Ocean-rim countries (e.g., Black et al. 2003; Gadgil et al. 2004; Cai et al. 2009; Li et al. 2016), and is even detected across the world due to atmospheric teleconnections (e.g., Saji and Yamagata 2003a; Guan and Yamagata 2003). Especially, extreme positive IOD (pIOD; warming over the WIO and cooling over the EIO) events usually cause disastrous floods and droughts in its surrounding regions. For instance, during the 1997 extreme pIOD event, massive floods struck East Africa (Webster et al. 1999; Hashizume et al. 2012), while devastating droughts and wildfires hit Indonesia and Australia (Abram 2003; Ummenhofer et al. 2009; Schott et al. 2009; Cai et al. 2014). Similar severe disasters occurred during the 2019 extreme pIOD event with the wettest rainy season in East Africa in recent decades (Wainwright et al. 2021) and more than 170,000 km^2 forests burned over Australia (Richards et al. 2020; Zhang et al. 2021a, b). These associated dramatic climate impacts call for urgent investigation into the physical processes of these extreme IOD events.

Despite that the relative importance of mechanisms responsible for the IOD remains debated, it seems to be

✉ Wenjun Zhang
zhangwj@nuist.edu.cn

[1] CIC-FEMD/ILCEC, Key Laboratory of Meteorological Disaster of Ministry of Education (KLME), College of Atmospheric Sciences, Nanjing University of Information Science and Technology, Nanjing 210044, China

[2] Department of Oceanography and International Pacific Research Center (IPRC), School of Ocean and Earth Science and Technology, University of Hawai'I at Mānoa, Honolulu, HI, USA

largely a consensus that the IOD is a relatively weak (i.e., damped) natural mode, which can usually be triggered by external drivers (e.g., Saji et al. 1999; Webster et al. 1999; Allan et al. 2001; Baquero-Bernal et al. 2002; Annamalai et al. 2003; Han et al. 2006; Francis et al. 2007; Stuecker et al. 2017). Previous studies have demonstrated that the El Niño-Southern oscillation (ENSO), the dominant coupled ocean–atmosphere climate phenomenon in the tropical Pacific, can exert its influences on the tropical Indian Ocean (IO) SST variability via adjusting the zonal Walker Circulation (e.g., Xie et al. 2002; Annamalai et al. 2003; Yang et al. 2015; Zhang et al. 2015; Stuecker et al. 2017). During an El Niño developing boreal summer and autumn, suppressed convection over the Maritime Continent typically induces easterly wind anomalies over the tropical IO, which favor the development of the pIOD by amplifying the WIO-EIO SST gradient (e.g., Schott et al. 2009; Luo et al. 2010; Zhang et al. 2015). However, the IOD has a complex relationship with the simultaneous El Niño conditions in the tropical Pacific due to El Niño's considerable diversity in its spatial pattern (Zhang et al. 2015). That is, the amplitude of eastern Pacific (EP) El Niño events is linearly correlated with IOD amplitude. However, there is no statistically significant correlation between the amplitude of central Pacific (CP) El Niño events and IOD amplitude. Instead, the zonal location of the central Pacific (CP) El Niño-associated SST anomaly maximum is correlated with IOD amplitude (Zhang et al. 2015).

In recent four decades, three extreme pIOD events that occurred in 1994, 1997 and 2019, were all concurrent with an El Niño development in the same year. However, the SST anomalies associated with these three El Niño events exhibited markedly different features in their magnitude and spatial structure in the tropical Pacific (e.g., Yang et al. 2021). The 1997 extreme pIOD coincided with an extreme El Niño with its SST anomaly center located in the eastern Pacific while the other two events were accompanied by moderate El Niño conditions with SST anomaly centers located in the central Pacific. There have been several discussions about the formation mechanisms of these extreme pIOD events (e.g., Saji et al. 1999; Rao and Yamagata 2004; Lu et al.2018; Du et al. 2012; Lu and Ren 2020). For instance, the thermocline warming in the western IO triggered by the westward propagating oceanic downwelling Rossby waves contributed to the 2019 pIOD development via altering the zonal SST gradient (Du et al. 2012). The interhemispheric pressure gradient (IHPG) anomaly across the Maritime Continent is also suggested to favor the growth of the 2019 pIOD (Lu and Ren 2020). Apart from the triggers mentioned above, a possible role of the Madden–Julian oscillation (MJO; Madden and Julian 1971), a prominent mode of intraseasonal (30–90 days) variability in the tropical atmosphere, has also been proposed to play an important role in IOD development and decay (e.g., Rao and Yamagata 2004; Han et al. 2007; Rao et al. 2009; Zhang et al. 2021a, b). Both observations and model results suggest that the intraseasonal wind anomalies associated with the MJO can influence IOD events via modifying surface turbulent heat fluxes and oceanic processes (e.g., Rao and Yamagata 2004; Han et al. 2006, 2007; Du et al. 2012). One previous study documented that westerly wind anomalies associated with suppressed MJO convection contributed to the termination of the 1994 pIOD event by exciting an anomalous oceanic downwelling Kelvin wave (Rao and Yamagata, 2004). Another recent study argued that the intraseaonal easterlies in May 2019 enhanced the WIO-EIO SST gradient by changing the surface heat fluxes and thereby initiated the 2019 pIOD event (Zhang et al. 2021a, b). So far, to what extent these external forcings, such as El Niño and MJO events, contributed to the three extreme pIOD events remains to be elucidated.

In this study, we will first examine possible differences of the oceanic and atmospheric conditions during these three extreme pIOD events. Possible contributions of external forcings will then be discussed to explain the extreme amplitude of these pIOD events. In the remainder of this paper, Sect. 2 introduces the data and methodology. In Sect. 3, the characteristics of the extreme pIOD events and the related large-scale atmosphere–ocean conditions are analyzed. Furthermore, we elaborate possible contributions of the MJO to the extreme pIOD events in Sect. 4. Discussions and major conclusions are illustrated in Sect. 5.

2 Data and methodology

In this study, global monthly SST anomalies are calculated from the Optimally Interpolated Reynolds SST version 2 (OISSTv2; Reynolds et al. 2002) data, with a horizontal resolution of $1^\circ \times 1^\circ$. The monthly mean potential temperature dataset on a 0.333° latitude and 1° longitude horizontal grid is taken from the NCEP Global Ocean Data Assimilation System (GODAS; Behringer and Xue, 2004). The precipitation data with a resolution of $2.5^\circ \times 2.5^\circ$ are provided by the Climate Prediction Center Merged Analysis of Precipitation (CMAP) (Xie and Arkin 1997). The monthly and daily mean atmospheric reanalysis data, including sea level pressure (SLP) and 850 hPa winds, are derived from the National Centers for the Environmental Prediction-Department of Energy (NCEP-DOE) Atmospheric Model Intercomparison Project-II reanalysis datasets (Kanamitsu et al. 2002). The interpolated daily mean outgoing longwave radiation (OLR) data on a $2.5^\circ \times 2.5^\circ$ horizontal grid are from the National Oceanic and Atmospheric Administration (NOAA; Liebmann and Smith 1996).

The Dipole Mode Index (DMI; Saji et al. 1999), as a measure of the IOD intensity, is defined as the SST anomaly

difference between the tropical WIO (10° S–10° N, 50°–70° E) and EIO (10° S–0°, 90° E–110° E). A pIOD event is defined when the standardized DMI is above 0.5 standard deviation, leading to the identification of eight pIOD events during the analyzed time period (1982, 1991, 1994, 1997, 2006, 2015, 2018, 2019). Among them, three are classified as extreme pIOD events (1994, 1997, 2019) considering that their standardized DMI is larger than 2.0 standard deviation. The skewness is used here to quantify the strength asymmetry of IOD (White 1980). The definition of the coefficient of skewness is:

$$a_3 = \frac{m_3}{(m_2)^{3/2}} \quad (1)$$

where, $m_k = \sum_{i=0}^{n} \frac{(x_i - \bar{x})}{N}$, x_i is the i th observation, $\bar{x}$ the mean and N the number of observations. We use the Climate Prediction Center's definition to select ENSO events based on a threshold of ± 0.5 °C of the Niño3.4 index (area-averaged SST anomalies over 5° N–5° S, 120°–170° W) for five consecutive months. Furthermore, EP and CP El Niño events are identified based on the EP and CP indices (EPI and CPI; Ren and Jin 2011), which are obtained by using a mathematic transformation of the Niño3 (area-averaged SST anomalies over 5° N–5° S, 90°–150° W) and Niño4 (area-averaged SST anomalies over 5° N–5° S, 160°E–150° W) indices. The El Niño events with EPI greater than CPI are considered as EP El Niño events whereas those with CPI larger than EPI are identified as CP El Niño events. Here, three EP El Niño events (1982, 1997, 2015) and ten CP El Niño events (1986, 1987, 1991, 1994, 2002, 2004, 2006, 2009, 2018, 2019) are identified, largely consistent with previous studies (e.g., Zhang et al. 2015, 2021a, b). In order to examine the relationship between the CP El Niño's zonal location and the IOD intensity, we measure the zonal location of the CP El Niño by the longitude of the maximum zonal gradient of the equatorial (2° S–2° N) averaged SST anomalies, following our previous studies (e.g., Zhang et al. 2014, 2015). This index can well capture the location of anomalous atmospheric convective motion west of the warm SST anomaly center. The daily real-time multivariate MJO indices (RMM1 and RMM2; Wheeler and Hendon 2004) are used to describe the intraseasonal oscillation (ISO) activity, which are accessed from the Australian Bureau of Meteorology (http://www.bom.gov.au/climate/mjo/).

Anomalies for all variables are calculated based on the climatological mean of the analysis period from 1982–2020, and the long-term linear trend is removed to avoid possible influence from global warming. When illustrating the possible contributions of MJO activity on extreme pIOD events on intraseasonal time scales, the annual cycle (mean and first three harmonics of climatological annual variation) is removed from the daily mean OLR and 850 hPa zonal wind anomalies, and the running mean of the centered 120 days is also subtracted to remove interannual signals (Wheeler and Hendon 2004). All statistical significance tests are performed based on the two-tailed Student's t test.

3 Characteristics of extreme pIOD events and their related oceanic and atmospheric features

Figure 1a displays the autumn (September–October–November, SON) DMI during the IOD mature phase for the period of 1982–2020. The IOD exhibits a remarkable year-to-year variability and positive skewness (0.91) with larger intensity during its positive than during its negative phase. The pIOD events feature positive SST anomalies in the western tropical IO and negative SST anomalies off the Sumatra-Java coast, accompanied with easterly low-level wind anomalies across the central to eastern equatorial IO (Fig. 1b). Consistent with previous studies, the pIOD events usually develop in early boreal summer, peak in autumn, and decay rapidly in winter (Fig. 1c). In contrast to normal pIOD events, extreme pIOD events exhibit a much stronger increasing rate of SST anomalies from summer to autumn.

To examine the possible uniqueness of oceanic and atmospheric variables during these events, we first show in Fig. 2 the SST anomaly patterns during the peak phase for the three extreme pIOD events. These extreme events display roughly analogous SST and wind anomaly patterns to the regression as shown in Fig. 1b, except for a larger magnitude of the SST and low-level wind anomalies. Specifically, we see similar SST anomalies in the tropical eastern IO; however, different SST anomaly patterns are evident in the western tropical IO. The positive SST anomaly centers during the 1994 and 2019 pIOD events are mainly located over the central to western IO away from the eastern African coast, with easterly wind anomalies prevailing over the central and eastern IO (Fig. 2a, c). In comparison, stronger SST warming occurred in the western tropical IO close to the eastern Africa coast during the 1997 pIOD event. The corresponding easterly wind anomalies are extended to the western part of the basin (Fig. 2b).

Figure 3 shows the time evolutions of subsurface ocean temperatures south of the equator (0°–10° S) for normal and extreme pIOD events from boreal summer to autumn. Here the region of 0°–10°S is chosen since the subsurface temperature in this region are sensitive to atmospheric wind anomalies due to the climatologically relatively shallow thermocline (e.g., Xie et al. 2002; Yang et al. 2015). For the normal pIOD events, the EIO thermocline starts to shallow in summer (Fig. 3a) and the ocean warming appears in central IO and strengthens in the following months (Fig. 3b).

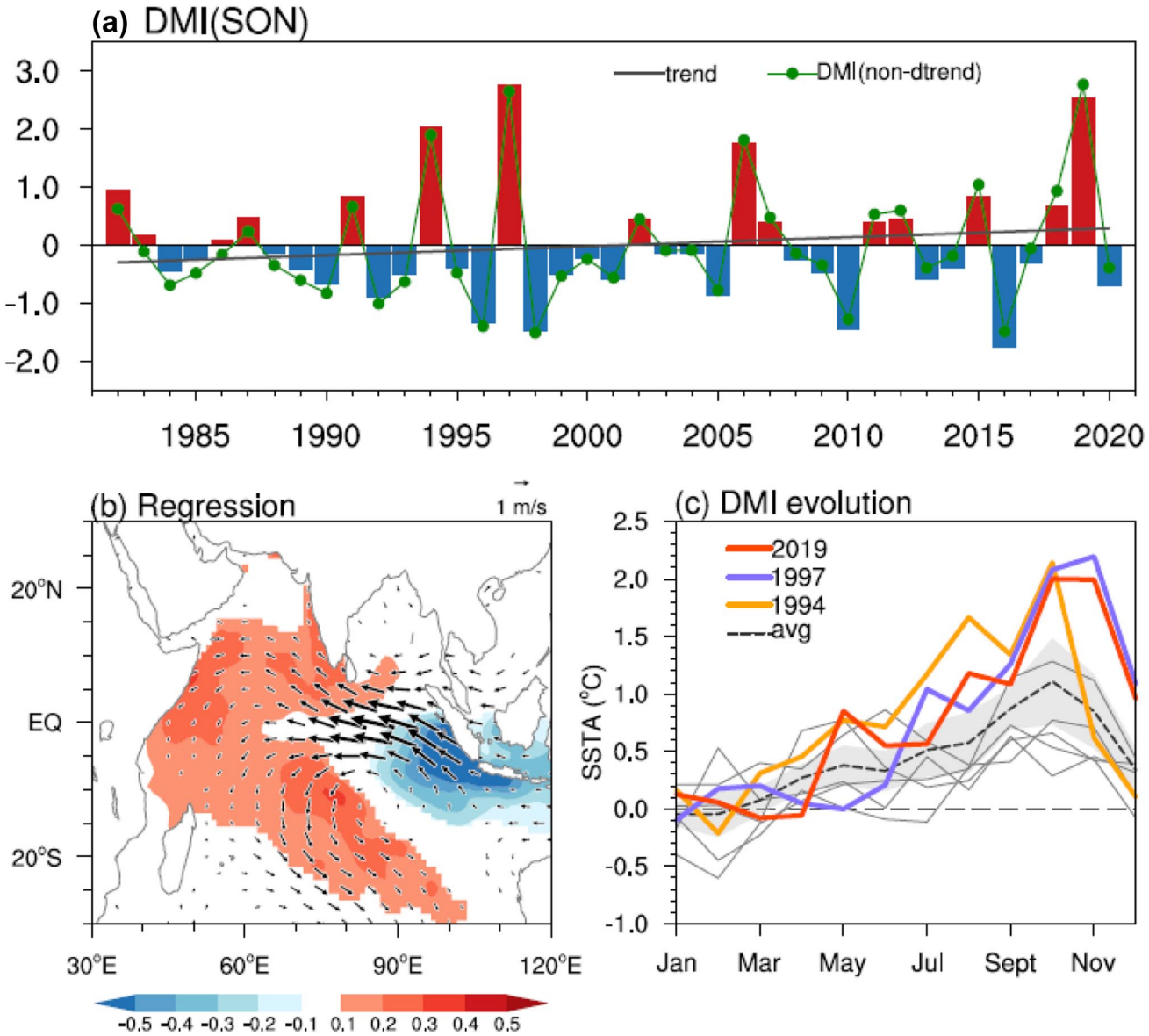


Fig. 1 **a** Time evolution of the detrended (bar) and non-detrended (green line) DMI during boreal autumn (September–October-November; SON) from 1982–2020. The black line denotes the trend. **b** Regressed SON SST anomalies (shadings; °C; only showing values that are statistically significant at the 95% confidence level) and 850 hPa wind anomalies (vectors; m/s; only showing values that are statistically significant at the 95% confidence level) onto the DMI. **c**) Monthly evolution of the DMI during the extreme pIOD events in 2019 (red line), 1997 (purple line), 1994 (orange line), remaining normal pIOD events (gray line), and their average (black dashed line). The light gray shading denotes 1 standard deviation of the DMI inter-event spread

In contrast to normal pIOD events, all three extreme pIOD events show much stronger temperature anomalies in summer and develop more rapidly in subsequent months (Fig. 3). Interestingly, the three extreme pIOD events exhibit a large diversity in their spatial structures, similar to the SST and low-level wind anomaly patterns (Fig. 2). A tripolar structure of subsurface temperature anomalies is detected for the 1994 and 2019 events, with warming in the central IO and cooling in the western and eastern part (Fig. 3c, d, g, h). In contrast, the 1997 pIOD event shows a dipolar structure of subsurface temperature anomalies, displaying warming and cooling in the western and eastern tropical IO, respectively (Fig. 3e, f).

As illustrated in the introduction, the pIOD events usually coincide with El Niño development. To explore whether the extreme pIOD events are closely associated with El Niño, we next show the oceanic and atmospheric conditions over the tropical Indo-Pacific region (Fig. 4). Consistent with previous studies (e.g., Schott et al. 2009; Luo et al. 2010; Zhang et al. 2015; Stuecker et al. 2017), a pIOD event is commonly

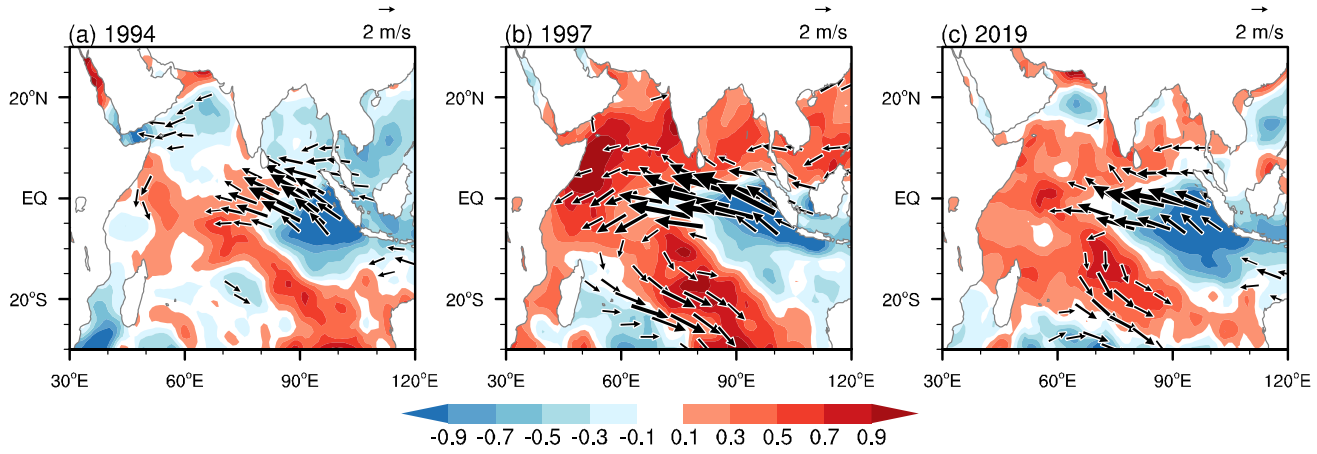


Fig. 2 Boreal autumn (SON) SST (shading; °C) and 850 hPa wind anomalies (vectors; m/s; only showing values exceeding 2 m/s) for the three extreme pIOD events

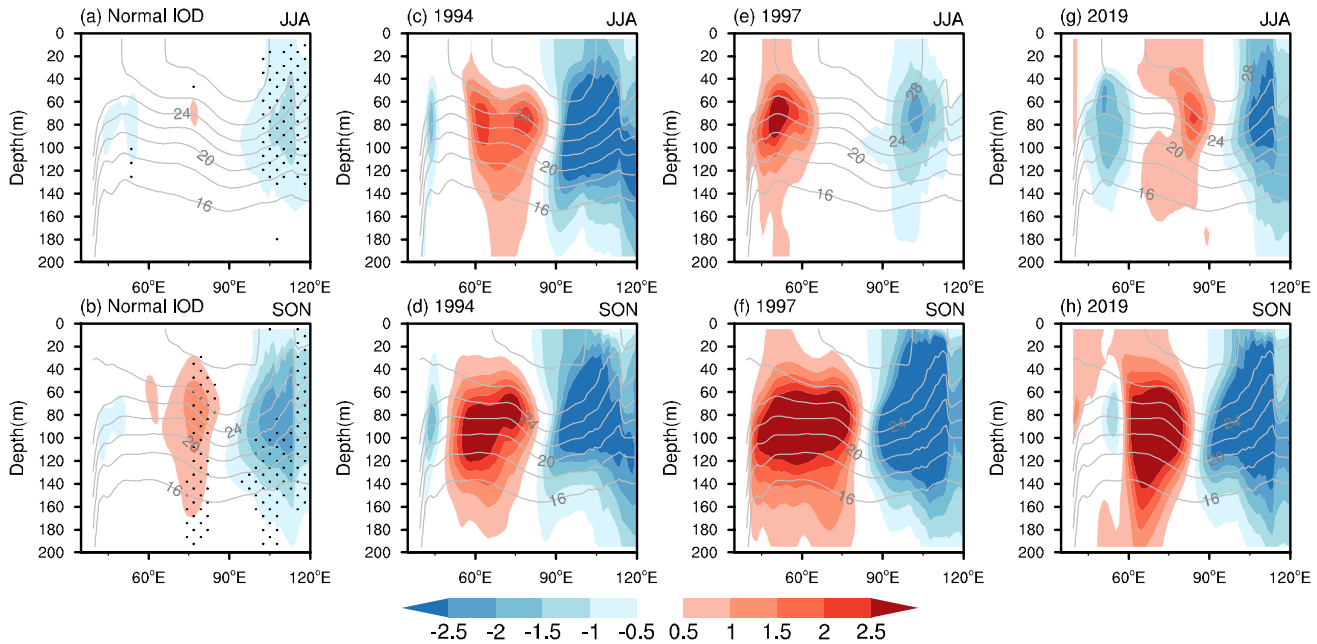


Fig. 3 Vertical structure of subsurface temperature anomalies (shading; °C) averaged between 0° and 10°S for normal pIOD events (1982, 1991, 2006, 2015, 2018) in June-July–August (**a**) and September–October-November (**b**). **c**-**d**, **e**–**f**, and **g**-**h** are same as **a**-**b**, but showing the anomalies for the 1994, 1997 and 2019 extreme pIOD events, respectively. The gray lines denote the seasonal climatological mean isotherms

accompanied by an El Niño developing state over the tropical Pacific based on the regression analysis (Fig. 4a, b). Correspondingly, westerly and southeasterly winds anomalies appear over the western-to-central Pacific and eastern IO, respectively. The easterly wind anomalies provide favorable conditions for the pIOD development mainly via the IO thermocline change. Similar low-level wind anomaly patterns occur over the eastern Indian and western Pacific Ocean for the three extreme pIOD events, despite of different intensity (Fig. 4c–h). In the Pacific, all the extreme pIOD events were concurrent with pronounced SST warming, but with a diversity in their spatial patterns. During 1997, a large SST warming exists in the central to eastern tropical Pacific (Fig. 4e, f), which is referred to as a typical EP El Niño based on our definition for EP and CP El Niño (see Sect. 2). However, the other two extreme pIOD events are accompanied with a SST warming in the central Pacific, which are identified as CP El Niño events (Fig. 4c, d, g, h).

Our previous study has suggested that the relationships of the pIOD with EP and CP El Niño events are quite different

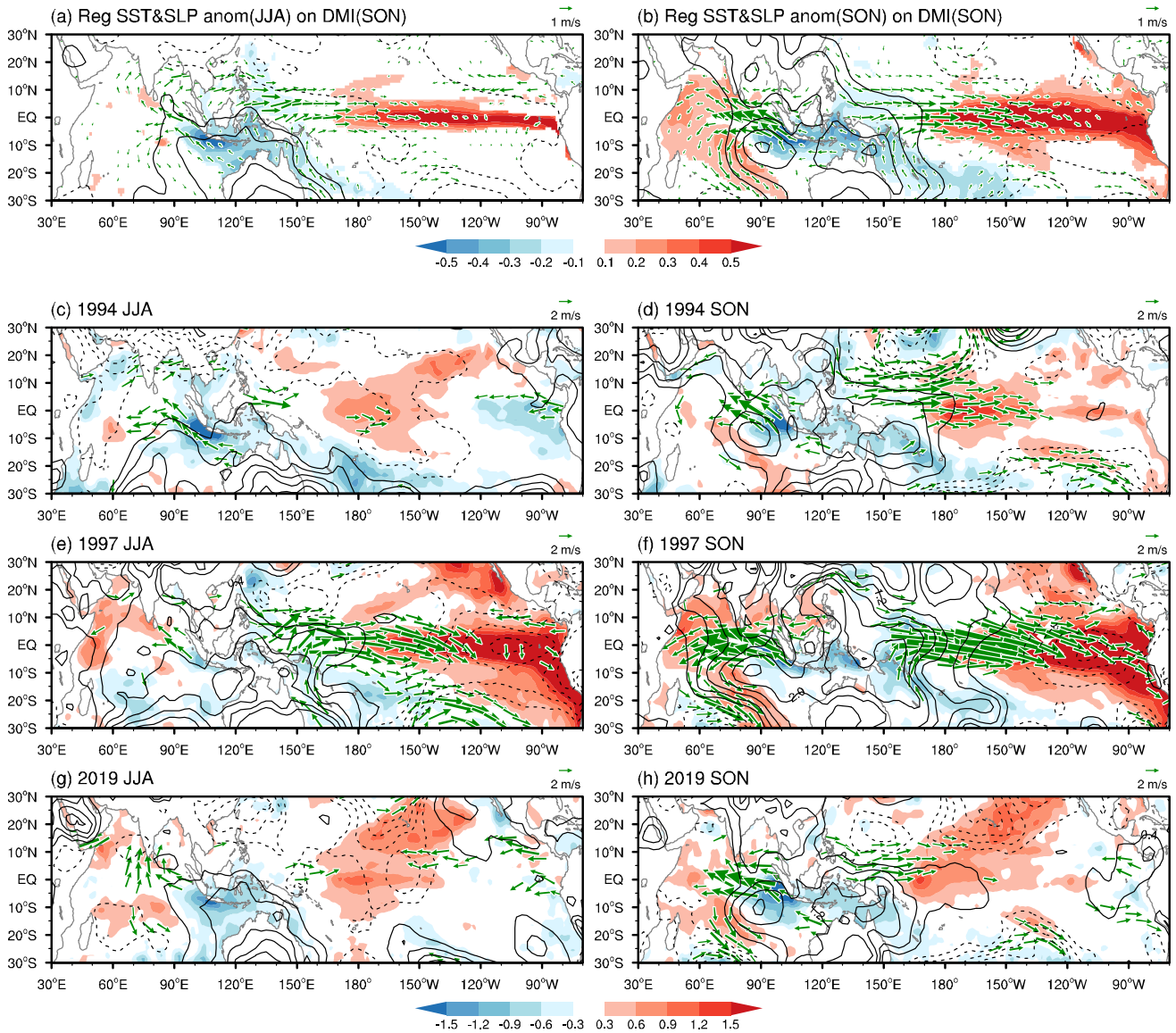


Fig. 4 Regressed June-July–August (JJA; **a**) and SON (**b**) SST anomalies (shading; °C; only showing values that are statistically significant at the 95% confidence level), SLP anomalies (contours; hPa; solid and dashed lines for positive and negative values, respectively), and 850 hPa wind anomalies (vectors; m/s; only showing values that are statistically significant at the 95% confidence level) onto the SON DMI. **c** SST anomalies (shadings; °C), SLP anomalies (contours; hPa; solid and dashed lines for positive and negative values, respectively), and 850 hPa wind anomalies (vectors; m/s; only showing values exceeding 2 m/s) in JJA 1994. **d** Same as **c**, but for SON 1994. **e**–**f** and **g**-**h** are same as **c**-**d**, but for the other two extreme pIOD events

(Zhang et al. 2015). We in Fig. 5 reexamine the linkage between El Niño and pIOD in autumn. To measure the different El Niño flavors, the Niño3.4 index is replaced by the EPI (Fig. 5b) and CPI (Fig. 5c), respectively, for the EP and CP El Niño events. A good linear correlation (R = 0.88) can be seen between the EP El Niño and pIOD (Fig. 5b; red dots) despite a small number (three) for EP El Niño events. This linear relationship can be confirmed by using a longer study period (1951–2013) and thereby larger sample size as done in our previous study (Zhang et al. 2015). In autumn 1997, the strongest recorded SST warming in the central to eastern Pacific since 1982 corresponds to the most extreme pIOD event. However, almost no linear relationship is found between the intensity of CP El Niño and pIOD (Fig. 5c; orange dots). In contrast, a significant linear relationship (r = 0.87, significant at the 99% confidence level) exists between the CP zonal location and pIOD intensity when excluding the 2019 pIOD event (Fig. 5d). The pIOD events tend to be stronger when the CP El Niño warming center shifts farther eastward. Among the nine CP El Niño

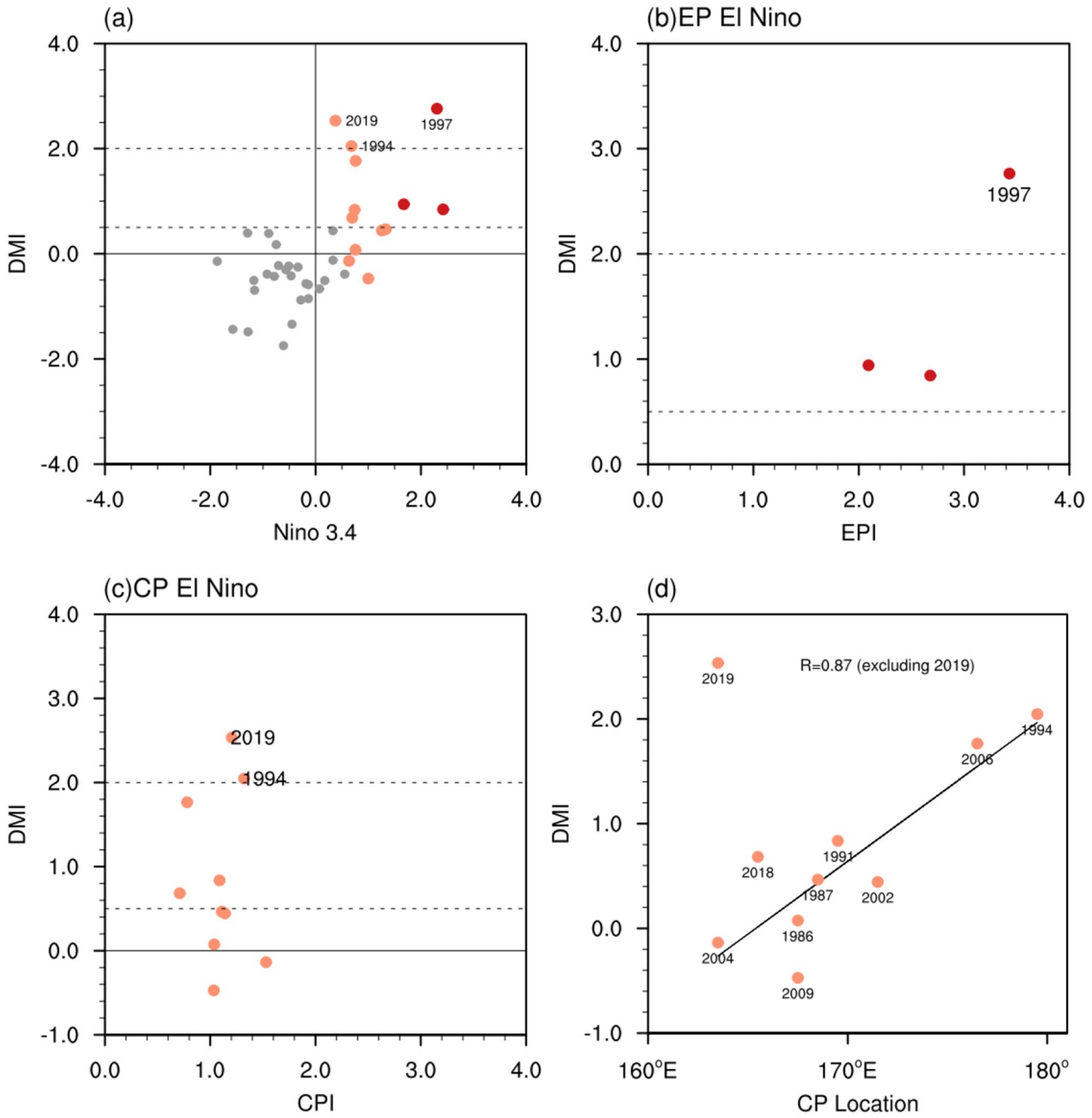


Fig. 5 **a** Relationship of the DMI with Niño 3.4 index during boreal autumn (SON). The orange and red dots denote the CP El Niño and EP El Niño events. **b**, **c** Same as **a**, but for the relationship of the DMI with EPI and CPI during EP El Niño and CP El Niño events. **d** Same as **a**, but for the scatterplot between the zonal location of CP El Niño and DMI (R = 0.87; excluding 2019)

events, the 1994 El Niño with the farthest eastward location corresponded to a large pIOD amplitude by modulating the atmospheric circulation in the Indian Ocean (Zhang et al. 2015). Thus, we conclude that the 1994 and 1997 extreme pIOD events were closely related to the Pacific warming.

Unexpectedly, the above conclusion is not valid for the extreme 2019 pIOD when the westernmost CP El Niño's SST anomalies are present in the tropical Pacific (Fig. 5d). To determine the reason for this exception, we show the monthly time evolution of the precipitation anomalies over the equatorial central and western Pacific in 2019 and compare it with other two extreme pIOD events (Fig. 6). The El Niño excited precipitation anomalies are normally located to the west of the SST warming center and are intensified

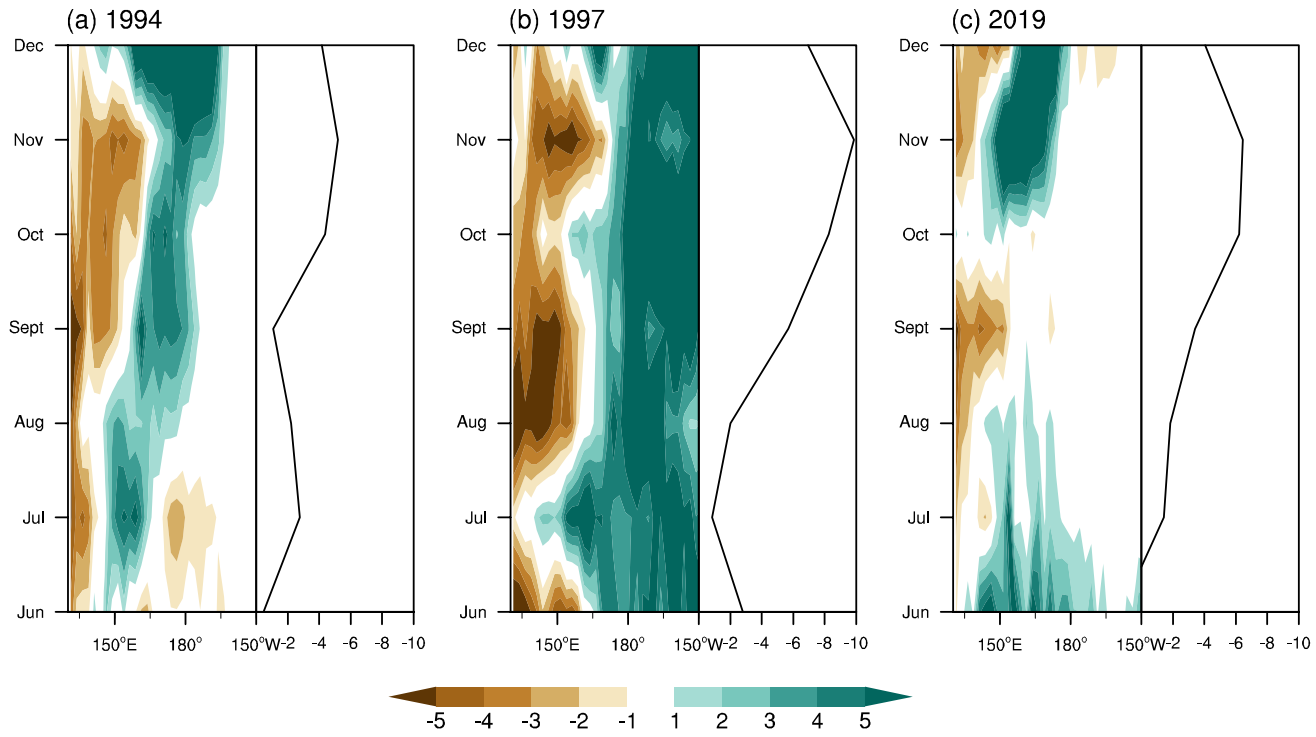


Fig. 6 Longitude-time diagrams of the composite equatorial western-central Pacific Ocean (2° S–2° N) precipitation anomalies (shading; mm/day) for the 1994 (**a**), 1997 (**b**), and 2019 (**c**) extreme pIOD events, respectively. Monthly equatorial Indian Ocean (60–90° E, 2° S–2° N) surface zonal wind anomalies are shown to the right of each plot

as SST anomalies increase, as observed during the extreme 1994 and 1997 pIOD events (Fig. 6a, b). During 2019, the weakly positive precipitation anomalies associated with the CP El Niño appear through June to August. Unlike during other pIOD events, the enhanced precipitation anomalies suddenly disappear over the equatorial central and western Pacific in September and October (Fig. 6c). This suggests that the role of the Pacific warming was largely absent for the development of the 2019 pIOD due to an apparent decoupling of the atmospheric response to the local SST anomalies in the tropical Pacific. Despite the absence of a remote forcing from the tropical Pacific, the SST gradient between WIO and EIO continues to grow along with the strengthened zonal easterly anomalies over the equatorial IO (Figs. 1c, 6c). This exceptional phenomenon inspires us to explore what other external forcing might have acted as a sort of "relay baton" in the rapid growth period (September–October) of the 2019 pIOD event.

4 Possible contribution of MJO to the extreme pIOD events during their mature phases

Superimposed on the dipole SST pattern in the IO, an abnormally persistent MJO activity was observed during September–October 2019, without an eastward-propagating features that traditional MJO events exhibit (Qi et al. 2021). Previous studies have shown that the zonal intraseasonal wind anomalies associated with the MJO can also affect IOD initiation and/or termination (e.g.,Rao 2004; Rao et al. 2009; Zhang et al. 2021a). During September–October 2019, a quasi-stationary active MJO stayed over the WIO (Phases 8&1) for 31 consecutive days (Fig. 7c), far beyond what is climatologically expected (Fig. 8a). In order to investigate a possible linkage between this unusual MJO activity and the underlying dipolar SST anomalies, we in Fig. 8b display the OLR and 850 hPa wind anomalies during the active MJO days in Phases 8&1 during early autumn of all the years excluding 2019. Enhanced and suppressed convection can be found over the central-western IO and EIO, respectively. The corresponding easterly wind anomalies prevail over the tropical IO, favoring the amplification of the WIO-EIO SST gradient. Similar convection and atmospheric circulation anomalies are observed during early autumn 2019 (not shown) and the main difference from other years is the much

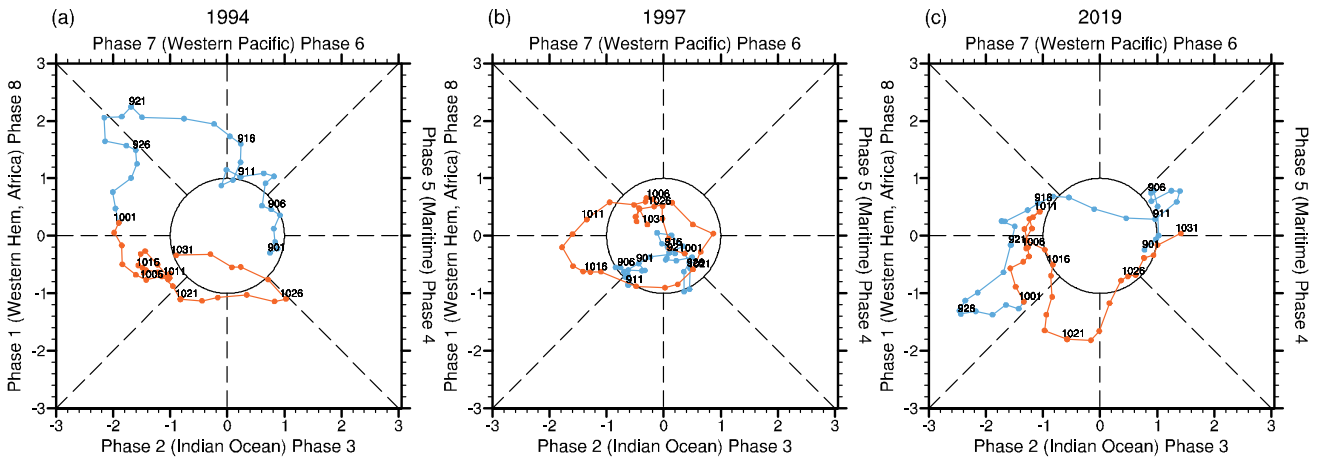


Fig. 7 The phase space diagram of the MJO from September 1 to October 31 for the three extreme IOD events. The blue and orange lines indicate the conditions in September and October, respectively. Numbers correspond to the date

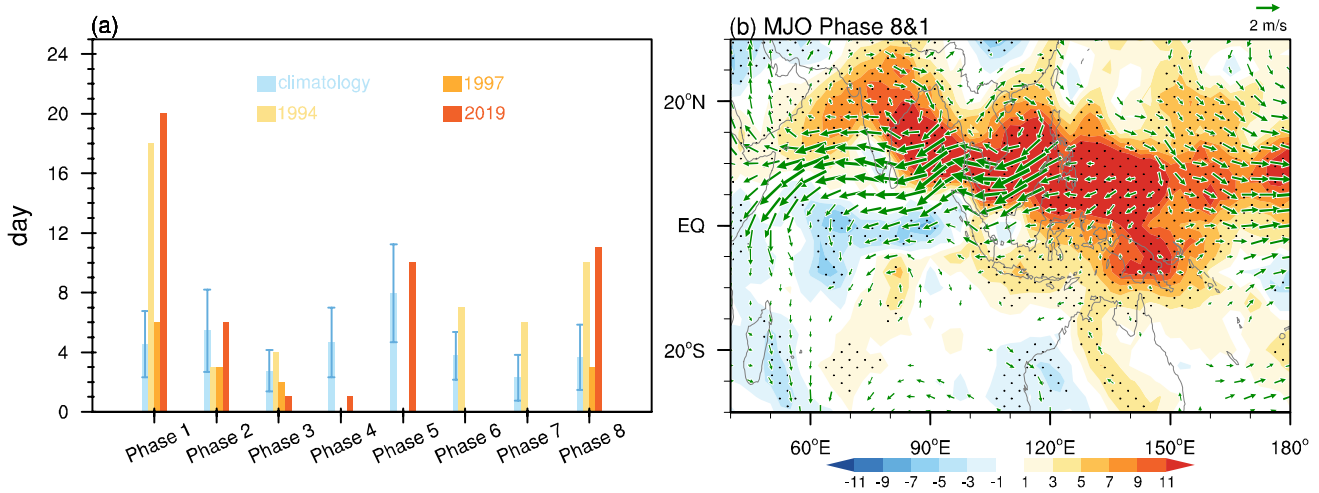


Fig. 8 **a** MJO active days in Phases 1–8 during September–October 1994 (yellow bar; day), 1997 (orange bar; day), 2019 (red bar; day), and the climatological mean (blue bar; day) with corresponding one standard deviation (error bars). The active days are selected when the MJO amplitude $(RMM1^2+RMM2^2)^{1/2}$ exceeds 1. **b** Composite OLR (shading; W/m^2) and 850 hPa wind anomalies (green vectors; m/s; only showing values that are statistically significant at the 95% confidence level) of active MJO days in Phases 8 and 1 during September–October for all years (1982–2020). Dots indicate the composite OLR anomalies that are statistically significant at the 95% confidence level

longer lasting active MJO over the IO (Fig. 8a). These persistent subseasonal easterly wind anomalies can strengthen the zonal easterly anomalies in absence of the remote CP El Niño forcing, further contributing to the amplifying the pIOD in its mature phase. Additionally, sustained MJO-associated downward motion over the equatorial western Pacific (Fig. 8b) may suppress precipitation anomalies relevant to the weak CP El Niño warming (Fig. 6c). We also examine the MJO activity in 1994 and 1997 (Fig. 7a, b). Similar to the 2019 case, quasi-stationary MJO activity was also observed over the WIO in 1994 (Fig. 7a), with 28 consecutive active days in Phases 8&1 (Fig. 8a). The associated subseasonal easterly wind anomalies can reinforce the IO background wind anomalies forced by the central Pacific warming, further intensifying the magnitude of the 1994 pIOD. In contrast, the MJO activities over the IO in early autumn 1997 were much weaker than during the other two years (Fig. 7b), suggesting only a minor effect of intraseasonal atmospheric forcing to the extreme amplitude of the pIOD. Previous statistical analyses have shown that CP El Niño years are typically concurrent with a larger growth rate of moisture and moist static energy over the MJO initiation area (i.e., Phases 8&1) compared to EP El Niño years (e.g., Hsu and Xiao 2017). Thus, the difference of the MJO convection between 1997 and other two years may be due to different El Niño types.

To highlight the importance of MJO associated intraseasonal zonal anomalies over the tropical IO on the extreme pIOD events, Fig. 9 shows the daily evolution of the equatorial 850-hPa total and intraseaonal (120-day high-pass filtered; HF) zonal wind anomalies over the IO, superimposed by the Niño 3.4 SST anomalies. From mid-September 1994 onwards, the total easterly anomalies prevailed over the IO, corresponding to a gradually enhanced CP warming and thus reduced zonal SST gradient in the tropical Pacific. The anomalous subseasonal easterly anomalies started to occur from mid-October to mid-November, contributing to the strengthened total zonal wind anomalies (Fig. 9a). A similar subseasonal evolution occurred in early autumn 2019, but with much stronger amplitude. The equatorial IO was mainly governed by the strong easterly wind anomalies during September–October on the intraseasonal time scale, which is the major component of the total wind anomalies (Fig. 9c). In contrast, the intraseasonal wind anomalies frequently oscillated up and down around zero during these two months in 1997, seemingly having minor effects on the mean total easterly anomalies. Thus, the strong total anomalous easterlies were dominantly contributed by the low-frequency variability associated with the Pacific warming (Fig. 9b).

Furthermore, the multiple linear regression is used to quantify the MJO's effect (Fig. 10). The reconstructed DMI based on the concurrent Niño 3.4 index and MJO active days in Phases 8&1 is highly correlated with the observation (R = 0.73; blue line; Fig. 10a) and the inclusion of MJO activities explain an additional 21% variance (statistically significant at 95% confidence level) of the September–October IOD variability for the entire period (i.e., 1982–2020). For the 1994 and 2019 extreme pIOD, the reconstructed DMI is predominantly contributed by MJO activities, while the super El Niño over the tropical Pacific is the main trigger for the 1997 case (Fig. 10b). These results suggest that extreme MJO activities besides the ENSO signal can also act to boost the development of the IOD events, especially in those three extremes positive IOD events.

5 Summary and discussion

Based on the observational analyses, we investigated in this study the effects of both El Niño and the MJO forcing in the three extreme pIOD events that occurred in 1994, 1997, and 2019. We demonstrated that the physical drivers for these three extreme pIOD events had notable differences. In autumn 1994, the CP warming gave rise to the anomalous subsidence near the Maritime continent and the associated low-level divergence triggered easterly anomalies over the equatorial IO, which favored the growth of pIOD. Simultaneously, the intraseasonal easterly anomalies associated with a slowly propagating MJO event enhanced the total mean zonal easterly anomalies and further promoted the development of the 1994 pIOD (Fig. 11a). During autumn 1997, almost no significant MJO activities were monitored over the IO. However, the strongly weakened Walker Circulation triggered by an extreme EP El Niño in the Pacific Ocean led to the equatorial easterly anomalies in IO, amplifying the WIO-EIO gradient rapidly (Fig. 11b). During the same time of the calendar year in 2019, the westmost located CP El Niño among all the CP El Niño events in our study period is expected to be accompanied by a normal pIOD based on the previous statistical results (Fig. 6b). However, this pIOD event developed into an extreme pIOD, and its amplitude was comparable to the 1994 and 1997 cases. The quasi-stationary MJO activitiy maintained over the WIO contributed to the vigorously growth of the pIOD. Concurrently, the sustained MJO convection suppressed the precipitation anomalies triggered by the CP El Niño warming, thus the El Niño forcing had only a minor effect on the pIOD event during autumn. The associated conclusions are summarized in the schematic diagrams shown in Fig. 11.

One may argue that without the CP El Niño forcing, the 2019 pIOD could have grown into an extreme pIOD via the local Bjerknes feedback, considering that the oceanic nonlinear zonal and vertical advection triggered by strong easterly wind anomalies can substantially strengthen IOD amplitude (e.g., Cai et al. 2014; Wang et al. 2020). Here we conduct a pacemaker experiment using the Geophysical Fluid Dynamics Laboratory (GFDL) coupled model version 2.1 (CM2.1) to examine whether the 2019 IOD can continue to develop via the local Bjerknes feedback. For previous 20 years and 8 months, the SST over the IO (30° S–30° N, 30°–130° E, with a 10° buffer zone) is restored as the observed anomalies in August 2019 plus monthly SST climatology from the long-term CM2.1 runs, and the ocean and atmosphere are fully coupled elsewhere. From September of the 21st year, the global SST is restored as the climatology with only the IO being fully coupled. The ensemble consists of 10 members, each starts with a slightly different initial condition. Experimental results show that the pIOD rapidly decays instead of continuing to develop in the following months (Fig. 12c), suggesting that the pIOD may not grow into the extreme pIOD only through the local Bjerknes feedback. Similar conclusions can also be derived by conducting similar experiments for the 1994 and 1997 pIOD events (Fig. 12a, b). Note that the rapidly decaying of these three pIOD in the CM2.1 may due to the strong Newtonian cooling caused by the overly strong IOD amplitude in this model (Yang et al. 2015). These results highlight the importance that external forcing plays for the development of extrem pIOD events. For the 2019 pIOD, the MJO-associated intraseasonal easterly anomalies played an important role on the pIOD development during autumn in the absence of a remote CP El Niño forcing.

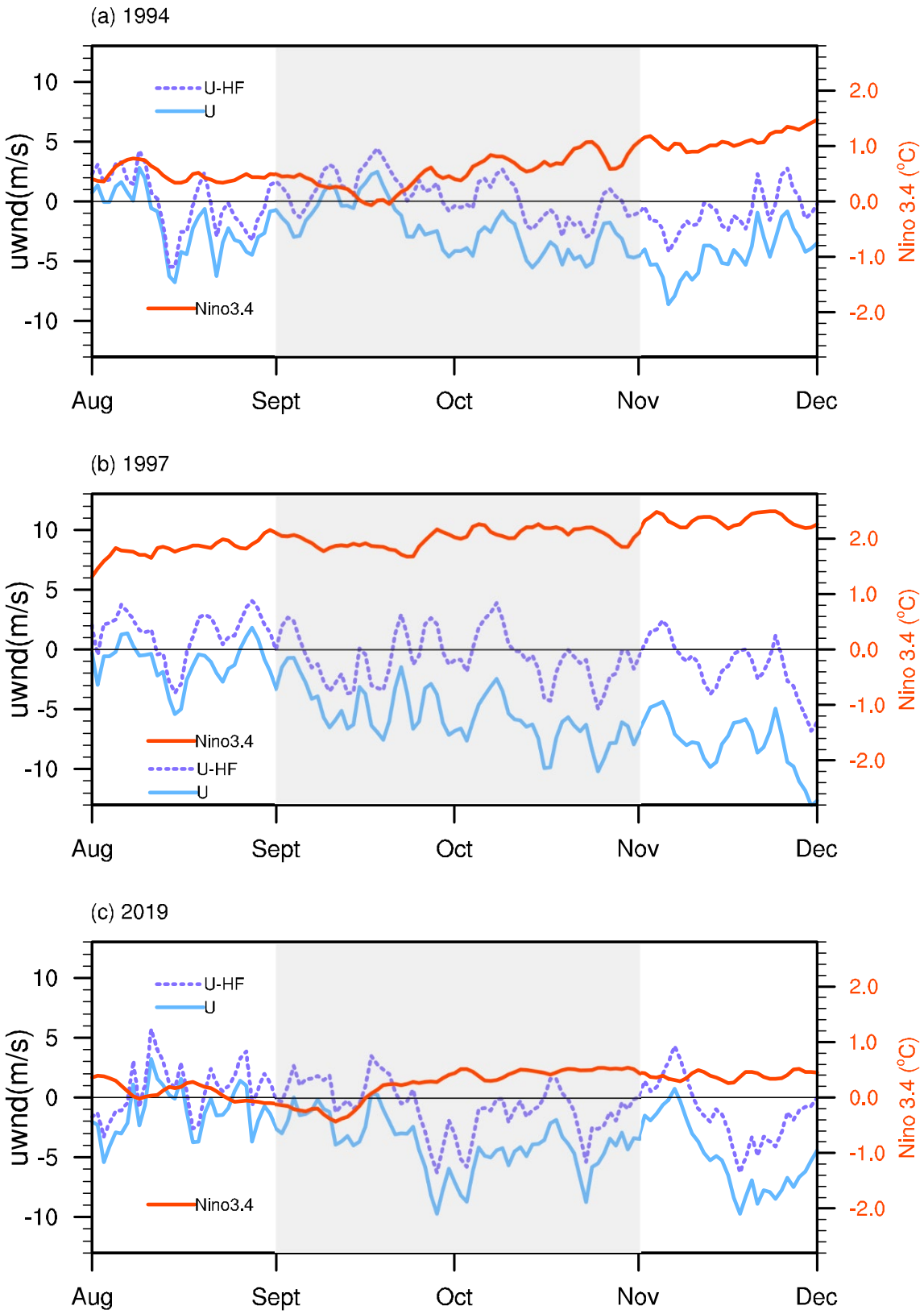


Fig. 9 Daily equatorial 850 hPa total (blue line; m/s; left *y*-axis) and 120-day high-pass filtered intraseasonal (purple line; m/s; left *y*-axis) zonal wind anomalies averaged over the Indian Ocean (60–90° E, 5° N to 5° S) for the three extreme IOD events from August to December. The SST anomalies over Niño 3.4 region are also displayed (red line; °C; right *y*-axis)

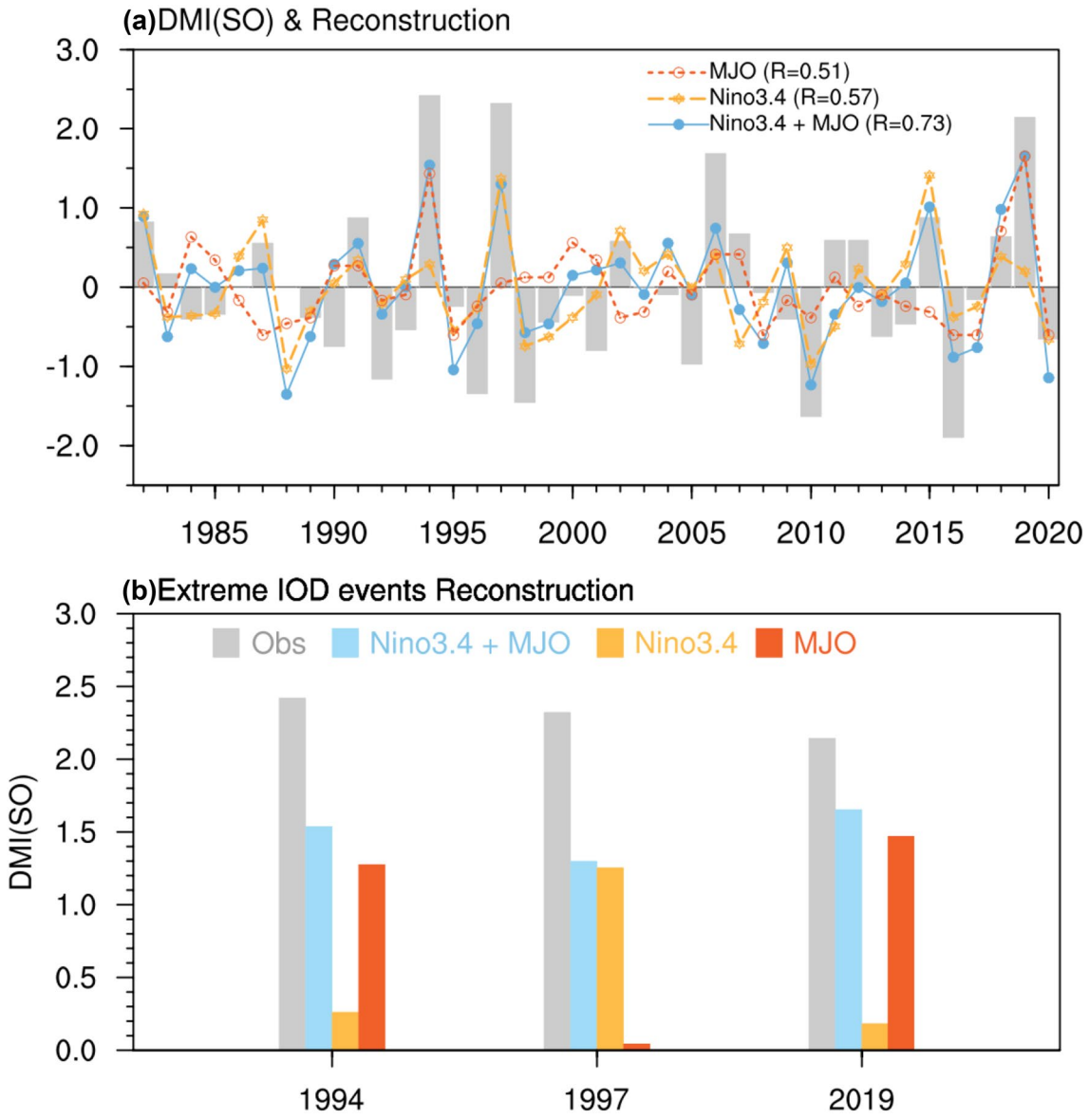


Fig. 10 **a** Time series of the observed DMI (gray bar), the reconstructed DMI based on the Niño3.4 index (orange line), MJO active days in Phases 8&1(red line) and based on both the Niño3.4 index and MJO active days in Phases 8&1 (blue line) during September–October from 1982–2020. The correlation coefficients between the observation and the reconstructions are also displayed. **b** The observed (gray bar) and reconstructed DMI based on both the Niño3.4 index and MJO active days in Phases 8&1 (blue bar) during September–October for the 1994, 1997 and 2019 extreme positive IOD events. The orange and red bars show the contribution of the Niño3.4 index and MJO active days in Phases 8&1, respectively

At present, the physical processes responsible for the stagnation of MJO events in early autumn 1994 and 2019 are still unclear. Usually, the MJO is a typical eastward propagation convection system with about 5 m/s velocity. While it exhibits a strong seasonality in its propagation feature. The typical eastward MJO features appear mainly during the cold seasons. In summer and autumn, the long resident MJO related convection is usually observed over the tropical Indian Ocean. Previous studies argued that the stalling feature of the MJO could be modulated by the local large-scale air-sea conditions via changing the wind and moisture patterns (e.g., Wilson et al. 2013; Sobel and Maloney, 2013). However, the relationship based on statistical analyses is complicated. For example, during the 1997 extreme IOD event, the MJO shows a normal propagation feature with a weakened amplitude. In contrast, during the 2019 extreme IOD event, the MJO exhibits an extraordinary persistent maintenance over the tropical Indian Ocean. It can be seen that the local air-sea condition cannot well explain the stalling feature of the MJO. So far, despite those relevant

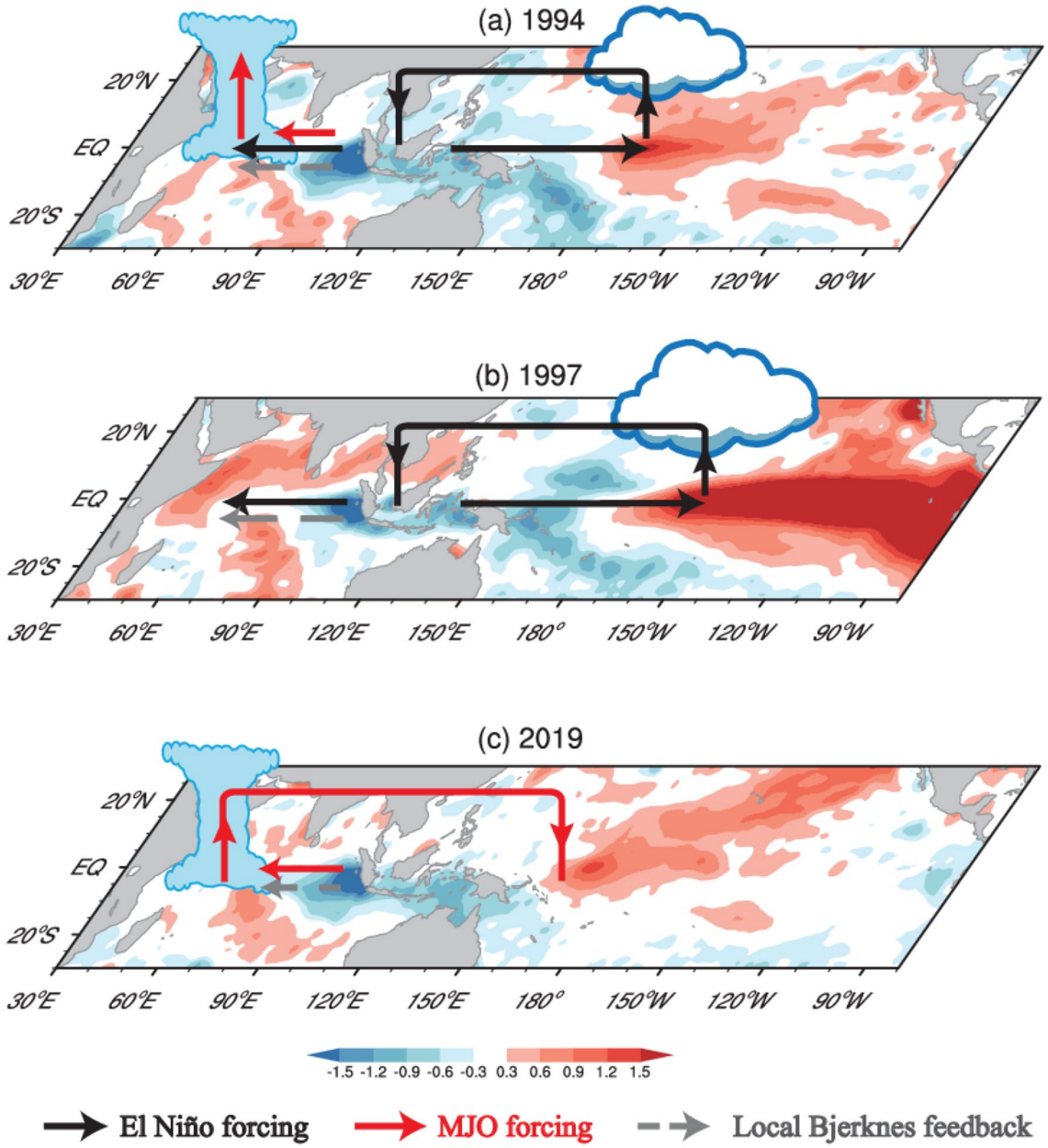


Fig. 11 Schematic diagrams of the mechanisms responsible for the three extreme IOD events during their mature phases (SO)

mechanisms are proposed, the MJO dynamics are not well understood including its initiation and propagation. The detailed controlling mechanisms deserve further investigations to improve our dynamical understanding of the quasi-stationary MJO events.

This study emphasizes the impacts of El Niño and MJO forcing on the three extreme pIOD events in their mature phases, without considering the influence of the background warming trend. The strengthening trend of the southeasterly wind anomalies off the Sumatra-Java coast induced by long-term SST change may also have had some contribution to the 2019 extreme pIOD through reinforcing the EIO cooling (Wang et al. 2020). So far, skilfull seasonal prediction of IOD events is still a challenge, especially for extreme IOD events (e.g., Luo et al. 2007; Zhao et al. 2019). The relationship between the ENSO and IOD has experienced a pronounced decadal change with their correlation coefficient substantially being weakened and becoming statistically insignificant since early 2000s, which has been attributed to the ENSO regime shift with more frequent CP ENSO events in recent decades (Teng et al. 2020). The independence between the intensity of CP ENSO and IOD is not conducive to a skillful seasonal prediction of the IOD, especially for the extreme pIOD events given that simulating the zonal

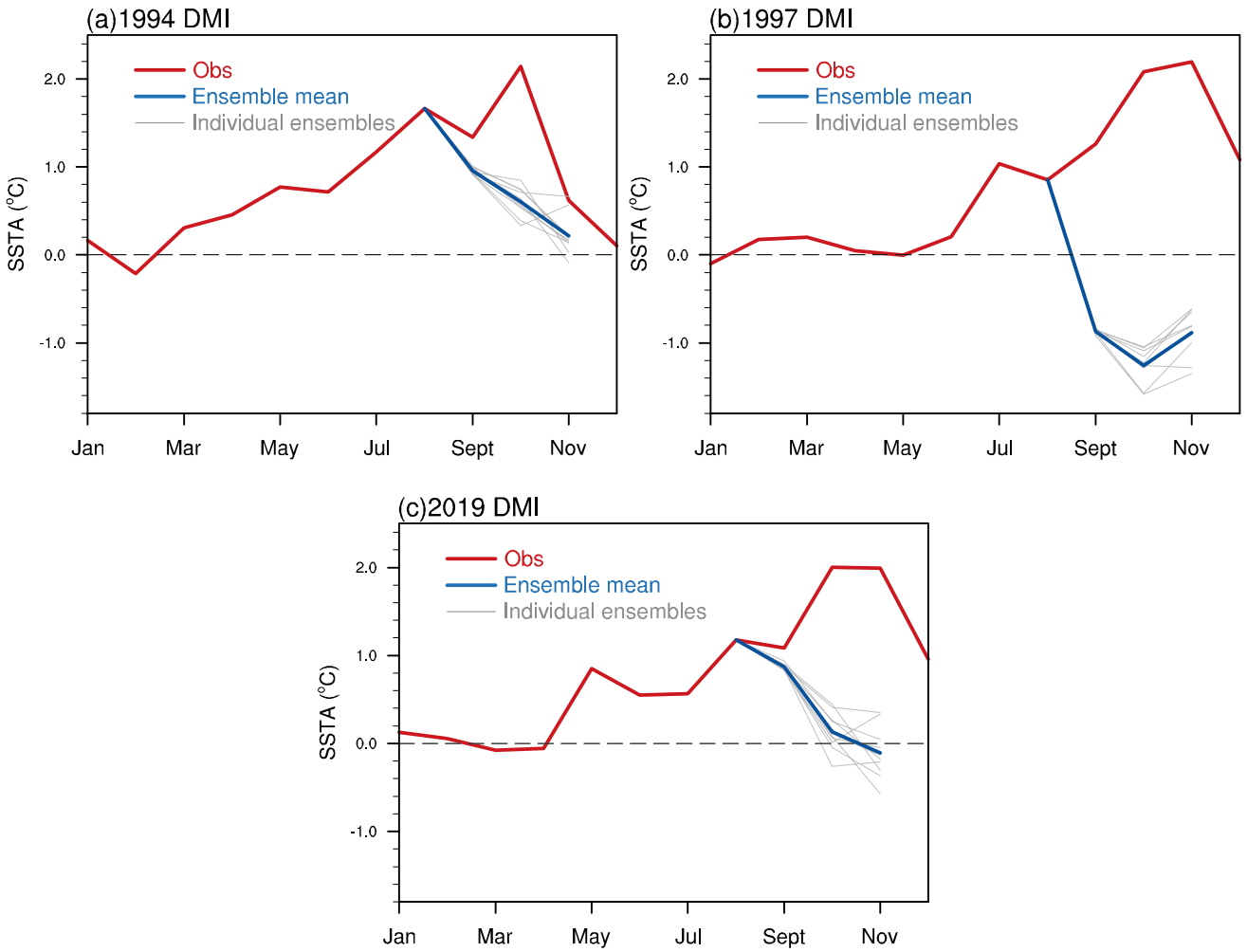


Fig. 12 Monthly evolution of the observed DMI (°C; red line) and model simulated DMI (°C; gray lines are 10 ensemble members and blue line is the ensemble mean result) when excluding the external forcing during the extreme pIOD events in 1994 (**a**), 1997 (**b**), and 2019 (**c**)

location of El Niño events is an additional challenge to simulating the correct amplitude of an event. Moreover, we have seen a sharp decrease in skillful lead time of ENSO predictability from about three season to one season in recent decades (McPhaden et al. 2011; Zhang et al. 2019), which works against skillful IOD prediction as well (Zhao et al. 2019). In addition, MJO activity is unpredictable beyond several weeks lead time in state-of-the-art subseasonal-to-seasonal prediction models (Lim et al. 2018). For instance, the real-time forecasts from the NCEP Climate Forecast System, version 2 (CFSv2) performed poorly in predicting the 2019 extreme pIOD (Fig. 9 in Zhang et al. 2021a, b). Larger efforts are required to improve model performances in accurately simulating Indo-Pacific atmospheric and ocean variability on multiple time scales to improve IOD predictability.

Acknowledgements This work was supported by the National Nature Science Foundation of China (42088101 and 42125501), and the Innovation Project of Jiangsu Province (KYCX21_0947). M.F.S. was supported by NOAA's Climate Program Office's Modeling Analysis, Predictions, and Projections (MAPP) program Grant NA20OAR4310445.

Funding The funding has been received from National Natural Science Foundation of China with Grant no. 42088101 and no. 42125501; Graduate Research and Innovation Projects of Jiangsu Province with Grant no. KYCX21_0947; Climate Program Office with Grant no. NA20OAR4310445.

Data availability The data used to support the finding are cited within the article.

Declarations

Conflict of interest The author declares that they have no competing interests.

References

Abram NJ (2003) Coral reef death during the 1997 Indian Ocean dipole linked to Indonesian wildfires. Science 301:952–955. https://doi.org/10.1126/science.1083841

Allan RJ, Chambers D, Drosdowsky W, Hendon H, Latif M, Nicholls N et al (2001) Is there an Indian Ocean dipole and is it independent of the El Niño-Southern oscillation? CLIVAR Exchanges 6:18–22

Annamalai H, Murtugudde R, Potemra J et al (2003) Coupled dynamics over the Indian Ocean: spring initiation of the Zonal Mode. Deep Sea Res Part II 50:2305–2330. https://doi.org/10.1016/S0967-0645(03)00058-4

Baquero-Bernal A, Latif M, Legutke S (2002) On Dipolelike variability of sea surface temperature in the tropical Indian Ocean. J Clim 15:11

Behringer DW, Xue Y (2004) Evaluation of the global ocean data assimilation system at NCEP: the Pacific Ocean. In: eighth symposium on integrated observing and assimilation systems for atmosphere, oceans, and land surface, AMS 84th Annual Meeting, Washington State Convention and Trade Center, Seattle, Washington, pp 11–15

Black E, Slingo J, Sperber KR (2003) An observational study of the relationship between excessively strong short rains in Coastal East Africa and Indian Ocean SST. Mon Weather Rev 131:21

Cai W, Cowan T, Sullivan A (2009) Recent unprecedented skewness towards positive Indian Ocean Dipole occurrences and its impact on Australian rainfall. Geophys Res Lett 36:L11705. https://doi.org/10.1029/2009GL037604

Cai W, Santoso A, Wang G et al (2014) Increased frequency of extreme Indian Ocean Dipole events due to greenhouse warming. Nature 510:254–258. https://doi.org/10.1038/nature13327

Du Y, Kai L, Wei Z, Wei-Dong Y (2012) The Kelvin Wave processes in the equatorial Indian Ocean during the 2006–2008 IOD events. Atmos Ocean Sci Lett 5:324–328. https://doi.org/10.1080/16742834.2012.11447007

Francis PA, Gadgil S, Vinayachandran PN (2007) Triggering of the positive Indian Ocean dipole events by severe cyclones over the Bay of Bengal. Tellus A 59(4):461–475. https://doi.org/10.1111/j.1600-0870.2007.00254.x

Gadgil S, Vinayachandran PN, Francis PA, Gadgil S (2004) Extremes of the Indian summer monsoon rainfall, ENSO and equatorial Indian Ocean oscillation. Geophys Res Lett 31:L12213. https://doi.org/10.1029/2004GL019733

Guan Z, Yamagata T (2003) The unusual summer of 1994 in East Asia: IOD teleconnections: IOD teleconnections. Geophys Res Lett 30(10):1544. https://doi.org/10.1029/2002GL016831

Han W, Shinoda T, Fu L-L, McCreary JP (2006) Impact of atmospheric intraseasonal oscillations on the Indian Ocean dipole during the 1990s*. J Phys Oceanogr 36:670–690. https://doi.org/10.1175/JPO2892.1

Han W, Yuan D, Liu WT, Halkides DJ (2007) Intraseasonal variability of Indian Ocean sea surface temperature during boreal winter: Madden-Julian Oscillation versus submonthly forcing and processes. J Geophys Res 112:C04001. https://doi.org/10.1029/2006JC003791

Hashizume M, Chaves LF, Minakawa N (2012) Indian Ocean dipole drives malaria resurgence in East African highlands. Sci Rep 2:269. https://doi.org/10.1038/srep00269

Hsu P-C, Xiao T (2017) Differences in the initiation and development of the madden–julian oscillation over the Indian Ocean associated with two types of El Niño. J Clim 30:1397–1415. https://doi.org/10.1175/JCLI-D-16-0336.1

Kanamitsu M, Ebisuzaki W, Woollen J, Yang S-K, Hnilo JJ, Fiorino M, Potter GL (2002) NCEP-DOE AMIP-II reanalysis (R-2). Bull Am Meteorol Soc 83:1631–1643. https://doi.org/10.1175/BAMS-83-11-1631

Li T, Wang B, Chang CP, Zhang YS (2003) A theory for the Indian Ocean dipole–zonal mode. J Atmos Sci 60:2119–2135

Li Z, Cai W, Lin X (2016) Dynamics of changing impacts of tropical Indo-Pacific variability on Indian and Australian rainfall. Sci Rep 6:31767. https://doi.org/10.1038/srep31767

Liebmann B, Smith C (1996) Description of a complete (interpolated) outgoing longwave radiation dataset. Bull Am Meteorol Soc 77:1275–1277

Lim Y, Son S-W, Kim D (2018) MJO prediction skill of the subseasonal-to-seasonal prediction models. J Clim 31:20

Lu B, Ren H-L (2020) What caused the extreme Indian Ocean dipole event in 2019? Geophys Res Lett 47:e2020GL087768. https://doi.org/10.1029/2020GL087768

Lu B, Ren H-L, Scaife AA et al (2018) An extreme negative Indian Ocean dipole event in 2016: dynamics and predictability. Clim Dyn 51:89–100. https://doi.org/10.1007/s00382-017-3908-2

Luo J-J, Masson S, Behera S, Yamagata T (2007) Experimental forecasts of the Indian Ocean dipole using a coupled OAGCM. J Clim 20:2178–2190. https://doi.org/10.1175/JCLI4132.1

Luo J-J, Zhang R, Behera SK et al (2010) Interaction between El Niño and extreme Indian Ocean dipole. J Clim 23:726–742. https://doi.org/10.1175/2009JCLI3104.1

Madden RA, Julian PR (1971) Detection of a 40–50 day oscillation in the zonal wind in the tropical Pacific. J Atmos Sci 28:702–708

McPhaden MJ, Lee T, McClurg D (2011) El Niño and its relationship to changing background conditions in the tropical Pacific Ocean. Geophys Res Lett. https://doi.org/10.1029/2011GL048275

Qi L, Ji Y, Zhang W (2021) Indispensable role of the madden-julian oscillation in the 2019 extreme autumn drought over eastern China. Geophys Res Atmos 126:e2020JD034123. https://doi.org/10.1029/2020JD034123

Rao SA (2004) Abrupt termination of Indian Ocean dipole events in response to intraseasonal disturbances. Geophys Res Lett 31:L19306. https://doi.org/10.1029/2004GL020842

Rao SA, Luo J-J, Behera SK, Yamagata T (2009) Generation and termination of Indian Ocean dipole events in 2003, 2006 and 2007. Clim Dyn 33:751–767. https://doi.org/10.1007/s00382-008-0498-z

Ren H-L, Jin F-F (2011) Niño indices for two types of ENSO: Niño indices for two types of Enso. Geophys Res Lett 38:L04704. https://doi.org/10.1029/2010GL046031

Reynolds RW, Rayner NA, Smith TM (2002) An improved in situ and satellite SST analysis for climate. J Clim 15:17

Richards L, Brew N, Smith L (2020). Australian bushfires—frequently asked questions: a quick guide. (Parliament of Australia, 2020) https://www.aph.gov.au/About_Parliament/Parliamentary_Departments/Parliamentary_Library/pubs/rp/rp1920/Quick_Guides/AustralianBushfires

Saji NH, Yamagata T (2003a) Possible impacts of Indian Ocean dipole mode events on global climate. Clim Res 25:151–169. https://doi.org/10.3354/cr025151

Saji NH, Yamagata T (2003b) Structure of SST and surface wind variability during Indian Ocean dipole mode events: COADS observations. J Clim 16:17

Saji NH, Goswami BN, Vinayachandran PN, Yamagata T (1999) A dipole mode in the tropical Indian Ocean. Nature 401:360–363. https://doi.org/10.1038/43854

Schott FA, Xie S-P, Mccreary JP (2009) Indian Ocean circulation and climate variability. Rev Geophys 47:549–549

Sobel A, Maloney E (2013) Moisture modes and the eastward propagation of the MJO. J Atmos Sci 70:187–192. https://doi.org/10.1175/JAS-D-12-0189.1

Stuecker MF, Timmermann A, Jin F et al (2017) Revisiting ENSO/Indian Ocean dipole phase relationships. Geophys Res Lett 44:2481–2492. https://doi.org/10.1002/2016GL072308

Teng YW, Zhang WJ, Liu C, Geng X, Qin CF (2020) Possible role of ENSO spatial pattern variation in interdecadal weakening of ENSO-IOD relationship. Acta Meteorol Sinica 78(2):210–220

Ummenhofer CC, England MH, McIntosh PC, Meyers GA, Pook MJ, Risbey JS, Gupta AS, Taschetto AS (2009) What causes southeast Australia's worst droughts? Geophys Res Lett 36:L04706. https://doi.org/10.1029/2008GL036801

Wainwright CM, Finney DL, Kilavi M et al (2021) Extreme rainfall in East Africa, October 2019–January 2020 and context under future climate change. Weather 76:26–31. https://doi.org/10.1002/wea.3824

Wang G, Cai W, Yang K et al (2020) A unique feature of the 2019 extreme positive Indian Ocean dipole event. Geophys Res Lett. https://doi.org/10.1029/2020GL088615

Webster PJ, Moore AM, Loschnigg JP, Leben RR (1999) Coupled ocean–atmosphere dynamics in the Indian Ocean during 1997–98. Nature 401:356–360. https://doi.org/10.1038/43848

Wheeler MC, Hendon HH (2004) An all-season real-time multivariate MJO index: development of an index for monitoring and prediction. Mon Weather Rev 132:1917–1932. https://doi.org/10.1175/1520-0493(2004)132%3c1917:AARMMI%3e2.0.CO;2

White GH (1980) Skewness, kurtosis and extreme values of Northern Hemisphere geopotential heights. Mon Weather Rev 108(9):1446–1455

Wilson EA, Gordon AL, Kim D (2013) Observations of the madden julian oscillation during Indian Ocean dipole events: IOD-MJO. J Geophys Res Atmos 118:2588–2599. https://doi.org/10.1002/jgrd.50241

Xie P, Arkin PA (1997) Global precipitation: a 17-year monthly analysis based on gauge observations, satellite estimates, and numerical model outputs. Bull Am Meteorol Soc 78:20

Xie SP, Annamalai H, Schott FA, McCreary JP Jr (2002) Structure and mechanisms of south Indian Ocean climate variability. J Clim 15(8):864–878

Yang Y, Xie S-P, Wu L et al (2015) Seasonality and predictability of the Indian Ocean dipole mode: ENSO forcing and internal variability. J Clim 28:16

Yang K, Cai W, Huang G et al (2021) Is Preconditioning effect on strong positive Indian Ocean dipole by a preceding central Pacific El Niño deterministic? Geophys Res Lett. https://doi.org/10.1029/2020GL092223

Zhang W, Jin F-F, Turner A (2014) Increasing autumn drought over southern China associated with ENSO regime shift. Geophys Res Lett 41:4020–4026. https://doi.org/10.1002/2014GL060130

Zhang W, Wang Y, Jin F-F et al (2015) Impact of different El Niño types on the El Niño/IOD relationship: relation of IOD with two-type El Niño. Geophys Res Lett 42:8570–8576. https://doi.org/10.1002/2015GL065703

Zhang W, Li S, Jin F et al (2019) ENSO regime changes responsible for decadal phase relationship variations between ENSO sea surface temperature and warm water volume. Geophys Res Lett 46:7546–7553. https://doi.org/10.1029/2019GL082943

Zhang L, Han W, Hu Z-Z (2021a) Inter-basin and multi-time scale interactions in generating the 2019 extreme Indian Ocean dipole. J Climate. https://doi.org/10.1175/JCLI-D-20-0760.1

Zhang W, Mao W, Jiang F et al (2021b) Tropical indo-pacific compounding thermal conditions drive the 2019 Australian extreme drought. Geophys Res Lett. https://doi.org/10.1029/2020GL090323

Zhao S, Jin F, Stuecker MF (2019) Improved predictability of the Indian Ocean dipole using seasonally modulated ENSO forcing forecasts. Geophys Res Lett 46:9980–9990. https://doi.org/10.1029/2019GL084196

Publisher's Note Springer Nature remains neutral with regard to jurisdictional claims in published maps and institutional affiliations.